Earth and Planetary Science Letters 399 (2014) 52–60

Contents lists available at ScienceDirect

Earth and Planetary Science Letters

www.elsevier.com/locate/epsl

Active water exchange and life near the grounding line of an Antarctic outlet glacier

Shin Sugiyama [a,*], Takanobu Sawagaki [b], Takehiro Fukuda [a,c], Shigeru Aoki [a]

[a] Institute of Low Temperature Science, Hokkaido University, Sapporo, Japan
[b] Faculty of Environmental Earth Science, Hokkaido University, Sapporo, Japan
[c] Graduate School of Environmental Science, Hokkaido University, Sapporo, Japan

ARTICLE INFO

Article history:
Received 16 January 2014
Received in revised form 30 April 2014
Accepted 3 May 2014
Available online 24 May 2014
Editor: P. Shearer

Keywords:
Antarctica
grounding line
basal melting
hot water drilling
outlet glacier
ice–ocean interaction

ABSTRACT

The grounding line (GL) of the Antarctic ice sheet forms the boundary between grounded and floating ice along the coast. Near this line, warm oceanic water contacts the ice shelf, producing the ice sheet's highest basal-melt rate. Despite the importance of this region, water properties and circulations near the GL are largely unexplored because in-situ observations are difficult. Here we present direct evidence of warm ocean-water transport to the innermost part of the subshelf cavity (several hundred meters seaward from the GL) of Langhovde Glacier, an outlet glacier in East Antarctica. Our measurements come from boreholes drilled through the glacier's ~400-m-thick grounding zone. Beneath the grounding zone, we find a 10–24-m-deep water layer of uniform temperature and salinity (−1.45 °C; 34.25 PSU), values that roughly equal those measured in the ocean in front of the glacier. Moreover, living organisms are found in the thin subglacial water layer. These findings indicate active transport of water and nutrients from the adjacent ocean, meaning that the subshelf environment interacts directly and rapidly with the ocean.

1. Introduction

The Antarctic ice sheet drains ice into the ocean through floating ice shelves and outlet glaciers, which account for 74% of the Antarctic coastline (Bindschadler et al., 2011; Rignot et al., 2011). Here, the flowing ice separates from the underlying bed at the grounding line (GL), entering the grounding zone, a km-scale transition zone between the grounded ice and the freely floating ice shelf in hydrostatic equilibrium (Fricker and Padman, 2006). Physical conditions beneath the grounding zone greatly influence the ice-sheet mass budget because the subshelf melt rate is greatest near the GL (Jacobs et al., 1992; Jenkins and Doake, 1991; Rignot and Jacobs, 2002). And, due presumably to ocean forcing (Dutrieux et al., 2014; Jacobs et al., 2011; Thoma et al., 2008), this basal-melt rate is thought to be increasing (Pritchard et al., 2012), leading to the recent ice mass loss in Antarctica.

The structure of the grounding zone influences the ice-sheet dynamics as well as the subshelf ocean circulation. The bed slope near the GL affects the stability of marine-terminating glaciers and ice streams (Weertman, 1974), with a reverse-sloping bed (i.e., lower elevation inland) thought unstable (Schoof, 2007; Jamieson et al., 2012). Moreover, bed geometry is a control of seawater intrusion and tidal mixing beneath the grounding zone, and thus affects the efficiency of heat transport from the ocean to ice-shelf base (Holland, 2008; MacAyeal, 1984). Researchers have used satellite remote sensing (Bindschadler et al., 2011; Rignot et al., 2011; Fricker and Padman, 2006; Rignot and Jacobs, 2002), and radar/seismic soundings (Anandakrishnan et al., 2007; Christianson et al., 2013; Horgan et al., 2013a, 2013b) to locate the GL and investigate the structure of the grounding zone, but have made few direct observations (Fricker et al., 2011; Powell et al., 1996). Because in-situ measurement data are unavailable, validation of remote sensing is difficult and the detailed structure of the grounding zone is poorly understood.

To investigate the physical structure and hydrological environment beneath the grounding zone of an Antarctic outlet glacier, we drilled boreholes near the GL of Langhovde Glacier. Using these boreholes, we directly measured subshelf water temperature, salinity, and current within several hundred meters from the GL as well as recorded video within the boreholes. Our data indicate active transport of warm water from the ocean to the grounding zone, and borehole video images reveal biological activities in the subglacial environment.

* Corresponding author. Tel.: +81 (0)11 706 7441.
E-mail address: sugishin@lowtem.hokudai.ac.jp (S. Sugiyama).

http://dx.doi.org/10.1016/j.epsl.2014.05.001

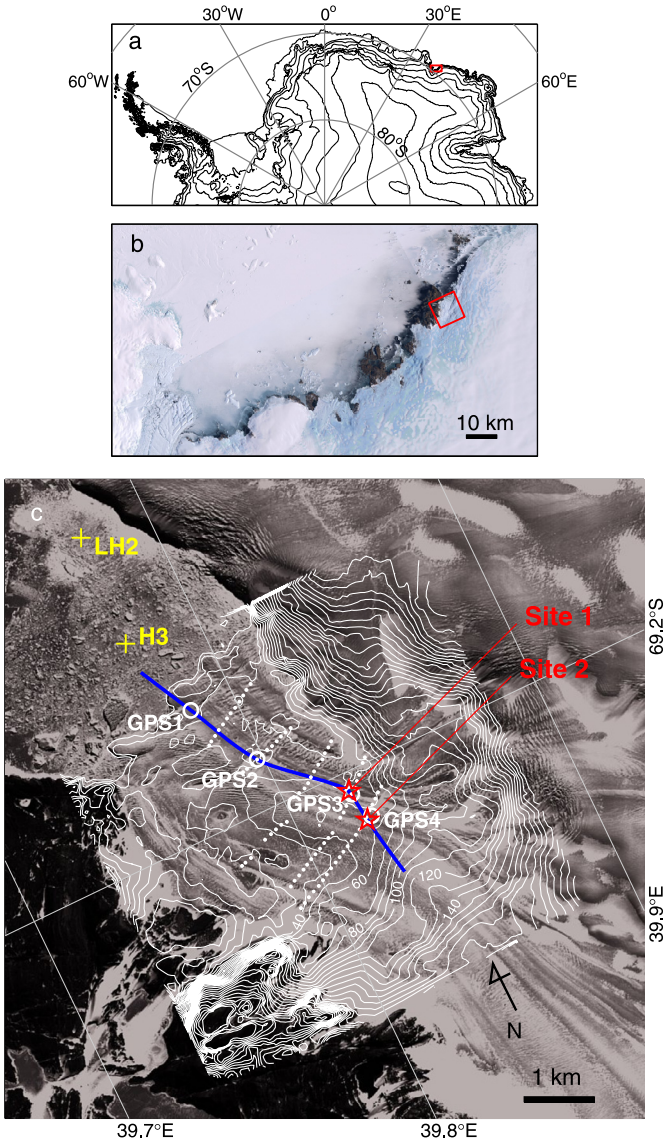

Fig. 1. The study area and measurement sites. (a) Antarctica and the location of Lützow–Holm Bay (red box, upper right). (b) Satellite image (Landsat Imagery Mosaic Antarctica) of Lützow–Holm Bay, covering the region of the box in (a). The dark color regions are ice-free land surface and the white region generally above the ice-free area is sea ice. The red box is the region in (c). (c) Locations of the drilling (stars), GPS (○), ice radar (●), and ocean measurement (+) sites. The blue line shows the location of the cross-section in Fig. 3. Ice surface contour intervals are 10 m. The background image is from ALOS PRISM, taken on 10 November, 2010. (For interpretation of the references to color in this figure legend, the reader is referred to the web version of this article.)

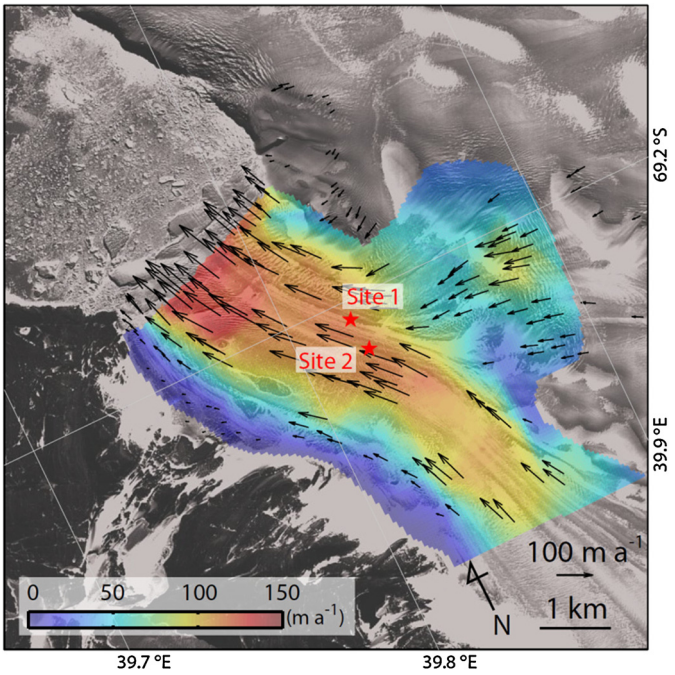

Fig. 2. Surface ice speed of Langhovde Glacier (color scale). The flow vectors were obtained from the displacement of surface features from 16 November 2006 to 19 November 2007. The color scale was determined by interpolating the flow vectors. (For interpretation of the references to color in this figure legend, the reader is referred to the web version of this article.)

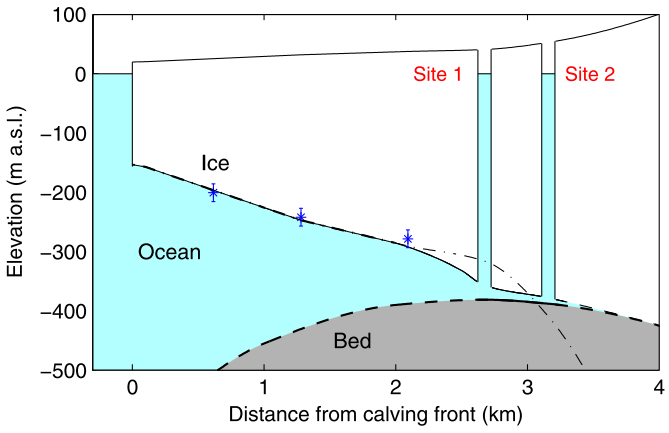

Fig. 3. Longitudinal cross-section of Langhovde Glacier along the blue line in Fig. 1(c). The ice bottom profile is based on ice radar data marked by ∗, as well as the hydrostatic equilibrium assumption (dash-dotted line) and the ice thicknesses at Sites 1 and 2. The bed elevation is based on the borehole measurements and known bathymetry near the calving front (Moriwaki and Yoshida, 1990). The ice bottom and bed elevation are extrapolated upglacier from Site 2.

2. Study site

Langhovde Glacier is a 3-km wide outlet glacier draining into Lützow–Holm Bay in East Antarctica (Fig. 1). It is a relatively small, but typical Antarctic outlet glacier. The lower 10 km of the glacier flows in a channel, which is bound by bedrock to the west and by relatively slowly moving ice to the east. In this region, ice flows at a rate up to 150 m a^{-1} as shown in Fig. 2 (see Section 3.4 for the method used to obtain the velocity map). According to our radar measurements (see Section 3.5) and a digital elevation model generated by a photogrammetric analysis of satellite images (Fukuda et al., 2014), the ice near the glacier terminus forms a floating ice shelf extending at least 2 km from the calving front. Ice in this region is 170–320 m thick, and the thickness and freeboard show the ice is in hydrostatic equilibrium (Fig. 3). Here, the glacier surface is flat and level in the lower reaches, but inland its slope increases at about 2.5 km from the terminus (Figs. 1(c) and 3). The floating ice is one to two orders of magnitude smaller in length than previously studied large ice shelves in West Antarctica (e.g. Ross, Filchner-Ronne, and Larsen Ice Shelves). The glacier terminus showed no significant retreating or advancing trend, i.e. frontal variation during 2000–2012 was within +300/−200 m (Fukuda et al., 2014). At the calving front, a bathymetric map (Moriwaki and Yoshida, 1990) shows a deep submarine trough with water depth of 602 m (and deeper offshore), but the seabed topography beneath the ice shelf is unknown.

3. Methods

3.1. Hot water drilling

In January 2012, we drilled boreholes near the GL of Langhovde Glacier. In most areas, ice was exposed on the glacier surface. At each of two sites, Site 1 at 2.7 km from the calving front and Site 2 at 3.2 km (Figs. 1(c), 2 and 3), we drilled two closely spaced holes (∼5-m apart) using a hot-water drill. The drilling was performed with a hot-water drill system previously used on mountain glaciers (Sugiyama et al., 2011; Tsutaki et al., 2013). The system consists of three high-pressure, hot-water machines (Kärcher HDS1000BE), 1/2-inch diameter hoses, and a winch system (Hubbard and Glasser, 2005; Sugiyama et al., 2010a). The mean drilling rate was 40 m h^{-1}. Thicknesses of both the ice and the subshelf water layer were determined to an accuracy of about ±1 m, using water temperature, salinity, and pressure profiles as described below.

3.2. Borehole measurements

We used a CTD (conductivity, temperature, and depth) profiler (IDRONAUT Ocean Seven 304) to measure water temperature, salinity, and depth to accuracy 0.005 °C, 7×10^{-3} mS cm^{-1} ($\sim 5 \times 10^{-3}$ PSU), and 0.5 m, respectively. Sampling intervals were 1 s. Water depth was derived from pressure by assuming fresh water density in the borehole, and uniform salinity (34.25 PSU) and temperature (−1.45 °C) below the ice. CTD measurements were repeated three times on 9 and 10 January 2012 at Site 1, and four times on 17 and 18 January at Site 2. All CTD casts were made 6–42 hours after the drilling. We used a current meter (JFE Advantec, AEM-USB; accuracy 1 cm s^{-1} and 2°) to measure water current and azimuth angles. The currents were measured on 10 January at Site 1 and on 17 January at Site 2. At every meter in depth, we recorded data for 1 minute with a 1-s sampling interval.

Water level in the borehole at Site 2 was measured every 10 minutes with a water pressure sensor (Geokon 4500S) installed at 5 m above the seabed. The accuracy of the measured pressure change was equivalent to several centimeters of water level. This pressure sensor was equipped with a thermistor sensor (Dale Electronics 1C3001-B3). We used this sensor to measure subshelf water temperature from 18 January 2012 to 29 January 2013. The thermistor resistance was measured and recorded every 30 minutes with a data logger (Campbell CR1000) powered by a solar panel. Data collection was interrupted from 9 February to 11 September 2012 because of data-logger failure. The thermistor temperature was calibrated by CTD measurements in the same borehole. Uncertainty due to the thermistor resistance linearization error and logger accuracy was about ±0.02 °C.

Two types of video cameras (Little Leonardo V500-LED and Looxcie LX2) were enclosed in pressure containers and lowered into the boreholes using a Kevlar string. Video files were downloaded when the cameras were retrieved after about 1 hr of recording. Depth was measured with a temperature and pressure sensor (JFE Advantec ATD-HR), which was lowered with the cameras.

Ice temperature was measured in the boreholes at 25–50-m intervals, using thermistor strings (Geokon, Model 3810) with an accuracy of approximately ±0.1 °C. The measurement was made in January 2013, one year after the installation. The measured temperature is used for estimating basal-melt rates.

3.3. Vertical ice motion and tides

Vertical ice surface motion was measured in the field at GPS1–4 (see Fig. 1(c) for the locations) with dual-frequency GPS (global positioning system) receivers (GNSS Technologies GEM-1 at GPS2 and Leica Geosystems System 1200 at the other sites). To operate, the GPS antennae were mounted on top of 1.5-m-long aluminum poles drilled into the ice. The GNSS receivers were run continuously, but to conserve power, the Leica receivers were run for just 30 minutes per hour. The GPS data were post-processed using a reference GPS station (GEM-1) fixed on the bedrock on the western flank of Langhovde Glacier (69°12′50″S, 39°44′38″E). The vertical motion of the poles was computed using GPS processing software (Leica Geo Office) with an accuracy of 3–5 mm (Sugiyama et al., 2010b). We processed the data in 1-hour time intervals, which were sufficient to resolve vertical ice motion in the study area. The computed coordinates were filtered using a Gaussian smoothing routine with ±1 hour time window.

Ocean tides were measured in front of the glacier at 69°10′41″S, 39°40′37″E, 4 km from the calving front. We used a waterlevel gauge (In-Situ's Level TROLL 500) to record sea-level change every 10 min with a resolution better than 0.01 m.

3.4. Ice velocity field

Ice surface velocity was measured by tracking glacial surface features on satellite images. The images came from panchromatic remote-sensing instruments for stereo mapping (PRISM), which was mounted on the Advanced Land Observation Satellite (ALOS) launched by JAXA (Japan Aerospace Exploration Agency). We identified more than 100 features (e.g., crevasses, water channels, melt ponds) and measured their displacement from 16 November 2006 to 19 November 2007 using GIS (geographical information system) software (ArcGIS, ESRI). The resolution of the images was 2.5 m and maximum error was estimated as 1.6 m a^{-1}. The velocity vectors and contours obtained by linear interpolation are shown in Fig. 2.

3.5. Ice thickness

Ice thickness was measured from 24 January to 9 February, 2012. We used a monopulse ice-penetrating radar system manufactured by Ohio State University, USA, which has been used to measure glacier thickness (e.g. Fukuda et al., 2011). Its central frequency is 5 MHz and its peak-to-peak output voltage is 1 kV (see Fig. 1(c) for the measurement locations). Based on pulse travel-times measured at the drilling site, where ice thickness is known from the boreholes, the wave propagation speed within the glacier is 1.81×10^8 m s^{-1}. This speed is near the upper bound of the values previously reported in Antarctica (Jezek et al., 1978; Bogorodsky et al., 1985). To obtain the ice-bottom elevation, we subtract the ice thickness from the surface elevation measured by kinematic GPS (Leica System 1200). Based on the wavelength and ambiguities in the return signal peaks, the ice-bottom elevation is accurate to ±15 m.

4. Results

4.1. Hot water drilling

The water level in the boreholes dropped to sea level when drilling reached the ice bottom, indicating connection to the ocean. Moreover, fluctuations of these water levels agreed with the ocean-tide levels measured in front of the glacier (Fig. 4(a)). The boreholes were inspected using the CTD profiler and borehole video cameras. We found a 24-m thick seawater layer beneath 398-m-thick ice at Site 1, and 10-m-thick seawater layer beneath 431-m-thick ice at Site 2 (Fig. 3). The seabed deepens upglacier at a slope of 0.8°. Given these ice thicknesses, the local ice-flotation level was 4.3-m below sea level (i.e., borehole water level) at Site 1, but

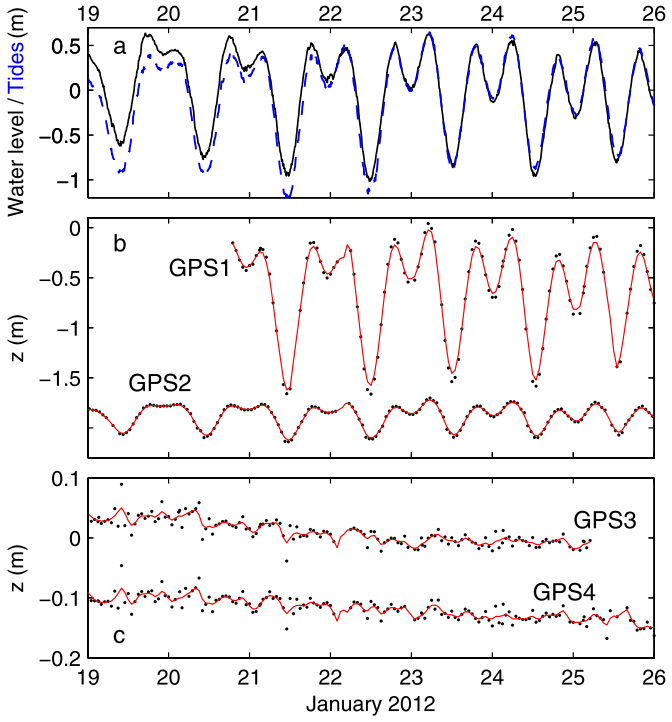

Fig. 4. Borehole water level, tides, and ice vertical motion. (a) Borehole water level variations at Site 2 (solid) and tidal amplitude measured 4-km from the glacier front (dashed). (b) Vertical glacier surface displacement at GPS1–2 (see locations in Fig. 1(c)). Hourly GPS coordinates (•) are filtered by Gaussian smoothing with ±1 hour time window (solid curves). (c) Same as (b) but for GPS3–4. GPS3 and GPS4 were within 100 m from Site 1 and 2, respectively.

3.6-m above sealevel at Site 2. Thus, as predicted for grounding zones, the ice at the drilling sites was not in hydrostatic equilibrium. The data indicate that the ice is above the hydrostatic equilibrium level at the upper site (Site 2) and below the same level in the lower site (Site 1). Such conditions are considered typical for a grounding zone configuration under the influence of ice flexure (Rignot et al., 2011; Smith, 1991; Stephenson, 1984). These observations demonstrated that the boreholes provided access to the innermost part of the subshelf cavity near the GL.

4.2. CTD and current measurements

CTD measurements revealed that this subshelf cavity was filled with homogeneous seawater at a temperature well above the freezing point. At these depths and salinity, the freezing temperatures are −2.151 and −2.166 °C at Sites 1 and 2 (Fujino et al., 1974), yet the measured mean in-situ temperature of the water columns were −1.450 °C at these sites, more than 0.7 °C above freezing. Both temperature and salinity slightly decrease towards the ice (Figs. 5(a) and (b)), but are otherwise fairly uniform throughout the water columns. The relatively warm temperature and uniformly distributed water properties suggest a high degree of water exchange with the adjacent ocean.

The temperature and salinity in the subshelf cavity equal, within seasonal variability (Ohshima et al., 1996), values measured previously in the nearby ocean (Ushio and Takizawa, 1993; Ohshima and Kawamura, 1994) (Figs. 6(a) and (b)). These previous measurements were performed within several kilometers from the calving front of Langhovde Glacier (Fig. 1(c)). The values are governed by large-scale oceanic dynamics on the continental shelf and slope. Onshore, the layer of Antarctic Surface Water (Whitworth et al., 1998) deepens, and entirely fills an approximately 500-m-thick upper layer in Lützow–Holm Bay (Ohshima et al., 1996). The vertical temperature and salinity gradients near the GL preserve the characteristics of the lower part of this embayment's Surface Water (Fig. 6(c)), which contains the warmth of underlying Modified Circumpolar Deep Water. Moreover, water temperature in the subshelf cavity showed seasonal variations as expected for the Surface Water; in particular, the annual temperature variations near the GL agreed with previous measurements at 20 km from the glacier (Fukuchi et al., 1985) (Fig. 7). These observations imply that the lower Surface Water actively refreshes the water in the subshelf cavity, swiftly removing subshelf meltwater from the grounding zone.

Water current measurements in the subshelf cavity support this hypothesis, showing flow speeds up to 3 $cm\,s^{-1}$ (Figs. 5(c) and (d)). At this rate, water beneath the drilling sites reaches the open ocean within one to two days. The observed current is slightly smaller than currents beneath large Antarctic ice shelves (Hattermann et al., 2012; Nicholls et al., 2006, 2012). The northeastward-to-eastward flow at Site 1 suggests cross-glacier flow, whereas the northwestward flow at Site 2 is consistent with outflow (Figs. 5(c) and (d)). The vertical shear of the flow speed is downward clockwise rotation near the seafloor at Site 1 (Fig. 5(c)), which is characteristic of Ekman boundary layer. However, agreement with the Ekman theory is less clear near the ice shelf bottom at Site 1 (Fig. 5(c)), and in both upper and lower boundary layers at Site 2 (Fig. 5(d)). The discrepancy from the theory is possibly due to the influence of uneven sea bed and ice-shelf bottom surfaces.

The ice motion should affect the currents as well. At the floating part of Langhovde Glacier at GPS1 and 2, the ice oscillates up and down up to 1.5 m (Fig. 4(b)). This vertical motion is consistent with the measured ocean tide (Fig. 4(a)), the amplitude of which is typical of that observed in the surrounding ocean (Padman et al., 2002). Thus, the tidally driven vertical ice-shelf motion likely pumps ocean water to the grounding zone, aiding the vertical mixing within the thin subshelf water layer (Holland, 2008; MacAyeal, 1984).

4.3. Borehole video observation

Consistent with the expected melting and measured currents, our borehole video cameras recorded images of dirty basal ice and water flow near the GL. Fine sediment inclusions occur in the basal ice nearer inland at Site 2 (Fig. 8(a) and Video 1), whereas the ice was clean at Site 1. This clean ice had probably melted off all of its basal silty ice during the ice flow from a region near Site 2 to Site 1 (see Section 5.1 for the basal melt-rate estimate). Consistent with this melt loss, the sea-floor consisted of fine sediment and decimeter-scale rocks with facets (Fig. 8(b)), which were most likely subglacial debris released from melting glacier sole. The cameras also revealed temporally nonuniform silty water currents near the bed (Video 2).

Life was also captured by video. A video from Site 1 shows a crustacean moving towards the camera's LED light (Fig. 8(c) and Video 3). This animal is probably *Glyptonotun antarcticus*, a commonly observed species in the Antarctic coast (Held and Johann-Wolfgang, 2005). It is similar to those discovered beneath the Ross Ice Shelf (Lipps et al., 1979), but is the first to be reported so close to a GL. The same site also had fish and krill-like animals (Video 4 and 5). Our observations strongly suggest that life in the Southern Ocean extends throughout the grounding zone. Riddle et al. (2007) and Gutt et al. (2011) observed a greater number and variety of organisms beneath ice further from the GL. Presumably, grounding zone processes (e.g., sediment deposition, occasional ice grounding) make this region less habitable than those reported in other ice shelves.

Microscopic organisms were also observed in water samples collected from the subshelf cavity near the bed at Site 1. The

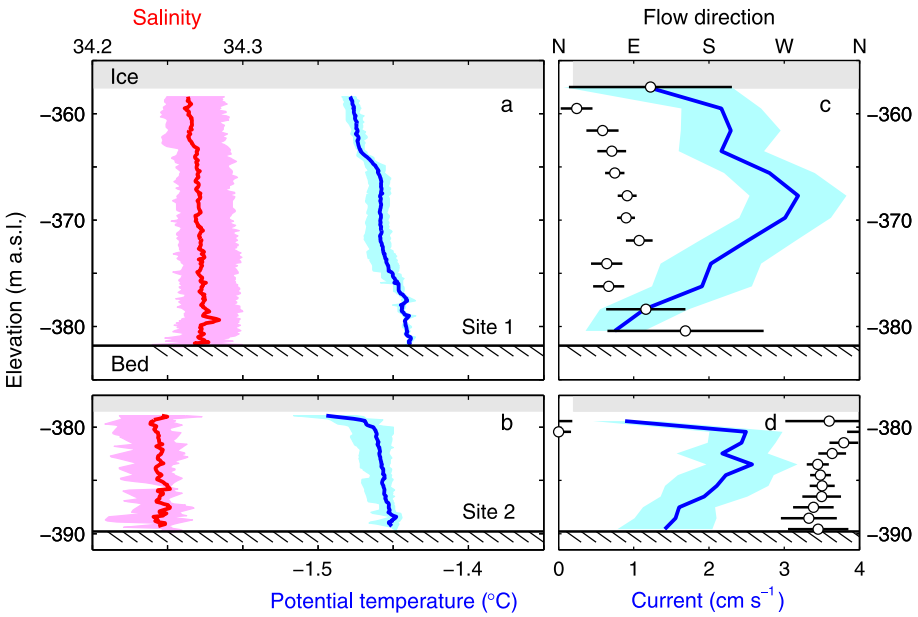

Fig. 5. Subshelf water properties measured at the drilling sites. (a) Temperature (blue) and salinity (red) at Site 1 and (b) Site 2. Mean values (solid line) and ranges (shaded band) are from measurements repeated three times on 9 and 10 January 2012 at Site 1, and four times on 17 and 18 January at Site 2. (c) Water current (blue) and flow direction (○) at Site 1 and (d) at Site 2. Mean values (solid line) and variation ranges (shaded band) are from 1-min measurements at each depth. The current and flow direction were measured on 10 January at Site 1 and on 17 January at Site 2. (For interpretation of the references to color in this figure legend, the reader is referred to the web version of this article.)

water included a number of phytoplankton cells such as diatom *Thalassiosira* sp. (Fig. 8(d)). The structures of the cells were preserved in very good conditions, suggesting that the phytoplankton were alive when the water was sampled, and thus they provide food for the larger animals. Moreover, because photosynthesis is not possible beneath the 400-m-thick ice, the phytoplankton must have recently come from the open ocean, consistent with our previous estimate of the water exchange rate. Thus, the subshelf current delivers not only heat, but also nutrients from the ocean.

5. Discussion

5.1. Basal melt rate

The measured current and relatively warm ocean water indicate substantial basal melting. Basal-melt rate $\dot{m}$ was estimated by solving the heat and salt flux balance equations at the ice–water boundary (Jenkins, 1991)

$$\rho_{\mathrm{fw}}\dot{m}L_{\mathrm{i}} - K_{\mathrm{i}}\left(\frac{\partial T}{\partial z}\right)_{\mathrm{b}} = \rho_{\mathrm{w}}c_{\mathrm{w}}\gamma_T(T - T_0) \tag{1}$$

$$\rho_{\mathrm{fw}}\dot{m}S_0 = \rho_{\mathrm{w}}\gamma_S(S - S_0) \tag{2}$$

where T (−1.45 °C), S (34.27 PSU at Site 1 and 34.25 PSU at Site 2), ρ_{w} (1027.5 kg m^{-3}), and c_{w} are the temperature, density, and specific heat capacity of the subshelf water, L_{i} and K_{i} are the latent heat of fusion and thermal conductivity of ice, and ρ_{fw} is the density of fresh water. The borehole temperature measurements gave an ice temperature gradient at the base of the ice $(\partial T/\partial z)_{\mathrm{b}}$ of 0.015 °C m^{-1}. The freezing temperature at the ice–ocean interface T_0 relates to salinity at the interface S_0 and pressure P (3.60 MPa at Site 1 and 3.82 MPa at Site 2) via

$$T_0 = -0.036 - 0.0499S_0 - 1.12\times10^{-4}S_0^2 - 0.00759P \tag{3}$$

(Fujino et al., 1974). The heat and salt transfer coefficients, γ_T and γ_S, for a smooth boundary are given by Jenkins (1991) as

$$\gamma_T = \frac{K^{1/2}U}{2.12\ln(K^{1/2}Re) + 12.5Pr^{2/3}} \tag{4}$$

$$\gamma_S = \frac{K^{1/2}U}{2.12\ln(K^{1/2}Re) + 12.5Sc^{2/3}}, \tag{5}$$

where $K = 2.5\times10^{-3}$ is the ice-shelf drag coefficient, Pr and Sc are the Prandtl and Schmidt numbers of seawater, and Re is the Reynolds number defined by $Re = UD/\nu$, with ν being the kinematic viscosity. The depth averaged velocity U and thickness D are 0.03 m s^{-1} and 12 m for Site 1, and 0.02 m s^{-1} and 5 m for Site 2, based on the field data. We solved Eqs. (1)–(3) for $\dot{m}$, using parameter values given by Jenkins (1991) unless otherwise stated above.

The above calculations give melt rates of 3.1 and 2.2 m a^{-1} at Site 1 and Site 2, respectively. The rates are sensitive to temperature, changing by 15% for a temperature change of 0.1 °C. Using the measured seasonal temperature variations from Fig. 7, the annual mean melt rates are estimated as 2.7 and 1.9 m a^{-1}. The range of rates is consistent with the thinning rate of 7.2 m a^{-1} estimated from the thickness change from Site 2 to Site 1 (−33 m) over the course of the ice flow (106 m a^{-1}), leaving some thinning to stretching ice flow and surface melting. Our estimate relies upon relatively short-period measurements, and thus contains uncertainty from tidal velocity variations. Given the relatively constant surface elevation observed for 2006–2012 over the floating part of Langhovde (Fukuda et al., 2014), the basal melting appears to be currently balanced with glacier flow and ice geometry.

Comparing to other regions, the estimated basal melt rates are similar to that for the inland margin of Ronne Ice Shelf (Jenkins and Doake, 1991) (4–5 m a^{-1}), less than those for large, thick Antarctic ice streams and glaciers (Rignot and Jacobs, 2002), but significantly greater than that measured with phase-sensitive radar near the GL of Rutford Ice Stream (Jenkins et al., 2006) (0.85 m a^{-1}). The rates are also less than the 7.0 m a^{-1} estimated for Shirase Glacier (Rignot et al., 2013) in Lützow–Holm Bay, which is several times larger and thicker than Langhovde Glacier. Shirase's greater melt rate is explained by the intrusion of warmer

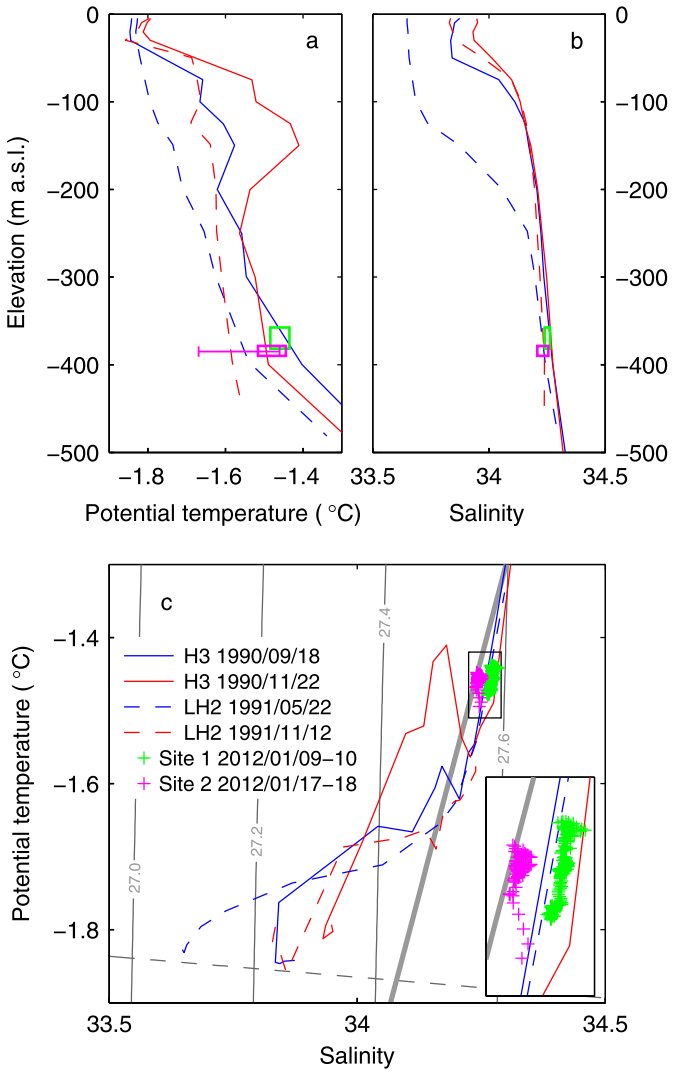

Fig. 6. Water properties beneath the drilling sites and in front of the glacier. (a) Water temperature measured by Ushio and Takizawa (1993) on 18 September (blue solid) and 22 November, 1990 (red solid) in front of the glacier at H3, and by Ohshima and Kawamura (1994) on 22 May (blue dashed) and 12 November, 1991 (red dashed) at LH2 (see locations in Fig. 1(c)). For comparison, the boxes are ranges of temperature and depth measured in the subshelf water layer at Site 1 (green) and Site 2 (magenta). The seasonal temperature variation range measured at Site 2 is indicated by the horizontal line. (b) Same as (a) except for salinity. (c) Potential temperature–salinity diagram of the data presented in (a) and (b). The inset shows the details of the clusters of + marks, which are measurements at Site 1 (green) and Site 2 (magenta). Also indicated by gray lines are the meltwater mixing line (thick solid), isopycnals (thin solid), and freezing temperature (dashed) referenced to surface pressure. (For interpretation of the references to color in this figure legend, the reader is referred to the web version of this article.)

Modified Circumpolar Deep Water to its base. Hence high basal melt rates are also expected in other glaciers of East Antarctica where warm water can reach shelf ice (Rignot et al., 2013).

5.2. Water mixing near the GL

The existence of a homogeneous water layer beneath the grounding zone can affect basal melting near the GL, which plays a critical role in the stability of marine-terminating outlet glaciers (Schoof, 2007). Heat exchange between ocean water and the ice shelf is relatively low when a melt-water-rich layer stratifies the upper part of the subshelf cavity. However, our observations indicate that water is well mixed near the GL and relatively warm

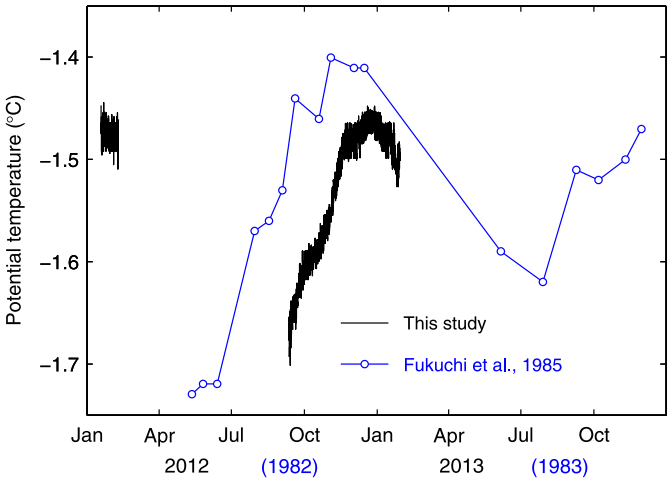

Fig. 7. Subshelf water temperature measured at Site 2 (black). The data-logger failed from 9 February to 11 September 2012, producing the observed data gap. Also plotted in blue is the 400-m-deep ocean temperature at 20 km from Langhovde Glacier measured from 1982 to 1983 (Fukuchi et al., 1985).

water is in contact with the ice-shelf base. Presumably, the subshelf tidal current stirs the water column, thus increasing the heat transport from ocean water to the ice shelf base.

Previous studies argued for a well-mixed water column near the GL (Holland, 2008; MacAyeal, 1984). These studies demonstrated that turbulence, due to tidal currents, destratifies the entire water column, forming a vertically uniform mixed zone within a certain distance from the GL. The mixed zone occurs where the melt rate is less than a critical melt rate $\dot{m}_c$ (Holland, 2008; MacAyeal, 1984):

$$\dot{m}_c = \frac{4\alpha K \mu U^3}{\beta g S D}, \tag{6}$$

where the water-layer thickness D, tidal-current speed U, and salinity S come from the borehole data at Site 1 and 2. We used the drag coefficient $K = 2.5 \times 10^{-3}$ as in Eqs. (4) and (5), the haline contraction coefficient $\beta = 8 \times 10^{-4}$ psu^{-1}, and the gravitational acceleration $g = 9.81$ m s^{-2}. For the other parameters in Eq. (6), we took into account uncertainties discussed in Holland (2008); the tidal energy expenditure for destratification $\alpha = 0.5$–1.5% and the tidal-velocity-variation parameter $\mu = 1.5$–3.0.

The resulting critical melt rate at Site 1 is 1.0–5.9 m a^{-1}, and that for Site 2 is 0.7–4.2 m a^{-1}, both of which are roughly equal to our estimated melt rates. Thus, the theory predicts our drilling sites were situated near the boundary of mixed and stratified water conditions. The observed vertical temperature gradient was small ($\sim 10^{-3}$ °C m^{-1}), but comparable to some of the measurements at greater distances from the GL beneath larger ice shelves (Hattermann et al., 2012; Nicholls et al., 2012). The slight stratification beneath Langhovde Glacier may represent the basal melt rate being similar to the critical melt rate. In addition to the parameter uncertainty, the critical melt rate is particularly sensitive to uncertainty in U. For more rigorous understanding of water mixing and melting conditions, a longer-term tidal current measurement beneath the grounding zone is required.

5.3. GL location and structure

Despite its importance for ice-sheet stability (Schoof, 2007), GL locations have been estimated only by remote (satellite and aircraft) and surface observations. A conventional method is to identify the GL with the change in surface slope from flat floating ice to relatively steep grounded ice (Bindschadler et al., 2011;

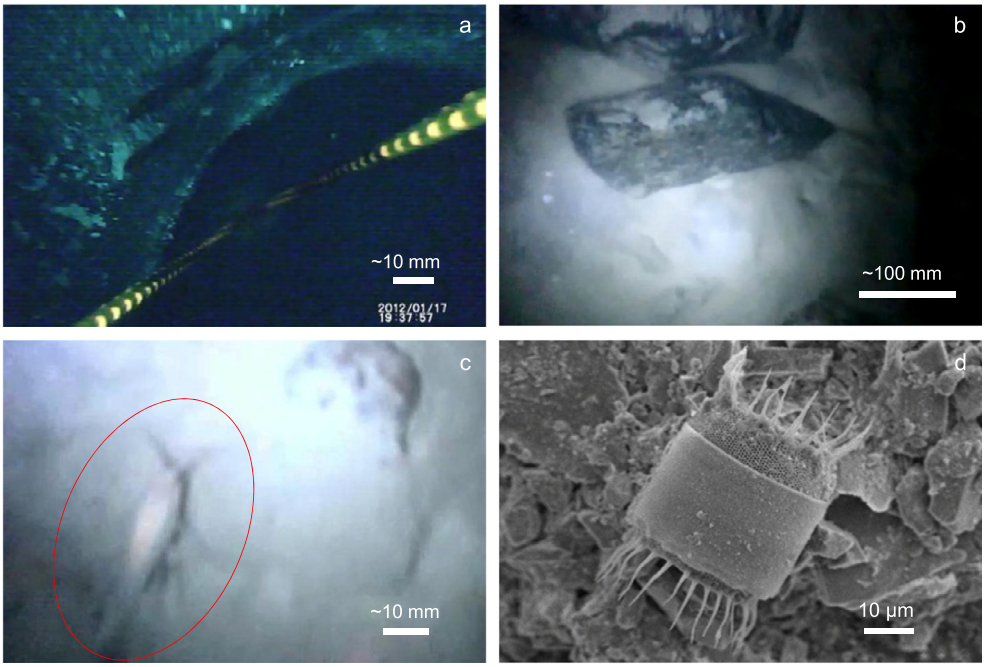

Fig. 8. Borehole and subshelf images, and a microscope observation of a subshelf-water sample. (a) View looking up borehole from subglacial water at Site 2. The large, dark circle shows the borehole (diameter about 150 mm). The white patches in the left side of the borehole are sediment inclusions. Lines with yellow dots are the cables holding the camera system. See also Video 1. (b) Sea floor at Site 1. The dark objects are faceted rocks, most likely melted out from the basal ice. (c) Crustacean observed on the sea floor at Site 1. See also Video 3. (d) Electron microscope image of phytoplankton cell found in water sample, 1-m above the sea floor at Site 1. (For interpretation of the references to color in this figure legend, the reader is referred to the web version of this article.)

Fricker and Padman, 2006). Applying this method to the surface slope marked in Fig. 3 (based on Fig. 1(c)), the GL of Langhovde Glacier would lie near Site 1. But clearly the GL lies further upstream than Site 2. Indeed, extrapolation of the ice bottom and seabed elevations suggests the GL is 830-m upglacier from Site 1. A more accurate technique is to measure tidal-induced ice-shelf vertical motion by interferometric analysis of synthetic aperture radar data (InSAR) (Rignot et al., 2011). Our GPS measurements showed 1.5 m of tidally driven vertical motion near the calving front at GPS1, with a progressively decreasing magnitude upglacier (Figs. 4(b) and (c)). No clear tidal signal was observed at Sites 1 and 2 (GPS3 and GPS4), even though these locations were underlain by a 10–24-m thick water layer. So, InSAR would likely put the GL further downstream. Thus, surface and remote sensing observations are not always reliable for determining the GL.

The important implications of our measurements are that seawater penetrates well upstream of the GL locations estimated by the standard methods and this seawater interacts with the basal ice over a greater area than previously thought. The difficulties in applying the standard methods arise from this glacier's relatively narrow width and its likely irregular bed shape near the GL. A slight ice surface rise just west of the drilling sites (Fig. 1(c)) suggests that geometry beneath the glacier is complex and ice is grounded in part. The horizontal distance to this possibly grounded region is less than 1 km, which is of the same order of magnitude as the local ice thickness. Being so near, the grounded ice exerts longitudinal and lateral stresses that are sufficiently large to influence the floating condition and the tidal ice motion at the drilling sites. These effects are important for relatively small and narrow outlet glaciers, which are commonly observed along the coast of East Antarctica. For instance, 45% of 175 outlet glaciers along the Antarctic coast of 90–170°E are 5 km or narrower at the terminus (Miles et al., 2013). Similar effects are expected even in a larger glacier when the bed geometry is complex and forms a narrow embayment along the GL. Our observation is also relevant to grounding zones of ice rises, which commonly occur in relatively small ice shelves in East Antarctica.

Comparing to Whillans Ice Stream, a larger and faster flowing ice stream in West Antarctica, we see some similarity and dissimilarity in the grounding-zone structure. Similar to Langhovde, Whillans has an ~10-m-thick water layer extending several kilometers downglacier from the GL (Christianson et al., 2013; Horgan et al., 2013a; 2013b). But at a certain location of Whillans, a wedge-shaped till deposit is reported in the grounding zone and thought to stabilize the GL position (Anandakrishnan et al., 2007; Alley et al., 2007). Langhovde appears to have no such deposit, which implies a relatively slow sediment deposition rate or a short occupation of the current grounding zone position. In addition to the melting of silty basal ice, sediment transport to the grounding zone can also occur by subglacial meltwater discharge, which was reported in other Antarctic outlet glaciers (Le Brocq et al., 2013; Stearns et al., 2008). However, given the lack of freshwater influence on the subshelf water properties (Fig. 5) and long-term temperature variations (Fig. 7), Langhovde likely has no subglacial discharge. Further, tidally driven vertical ice motion was small near the GL of Langhovde in contrast to the observations in Whillans (Horgan et al., 2013a). The lack of vertical ice motion suggests minimal influence of tidal flexure on ice flow and subglacial hydrology.

The measured shallow water layer beneath Langhovde Glacier would have formed (assuming hydrostatic equilibrium) with only several meters of ice-surface elevation change. Given that such small changes can drive rapid melting in outlet glaciers, accurate measurements and long-term monitoring on the grounding zones in Antarctica should receive more emphasis.

6. Conclusions

We reported in-situ measurements and video camera observations beneath the grounding zone of an East Antarctic outlet glacier. The measurements were carried out in the boreholes drilled near the GL of 398–400-m thick Langhovde Glacier. Be-

neath the grounding zone, we found a thin (10–24 m thick) subglacial seawater layer penetrating upstream of the estimated GL (from changes in the surface slope). Relatively warm (0.7 °C above freezing) homogeneous water fills the subshelf water cavity. Water temperature and salinity are roughly equal to those previously measured in front of the glacier. These measurements suggest active water transport from the open ocean to the innermost part of the subshelf environment. Basal melt rate near the GL was estimated as 2.2–3.1 $m\,a^{-1}$, based on the temperature and current obtained by the borehole measurements. The boreholes also revealed a variety of animals living in the thin water layer beneath the grounding zone. These findings provide key information to better understand the ice-sheet–ocean interaction, biodiversity in the polar ocean and the structure of Antarctic ice-sheet margins.

Acknowledgements

We thank M. Shirahama, K. Higuchi, and other members of the field campaign at Langhovde Glacier in 2011/2012 for their help on the glacier. Thanks are also to the 53rd Japanese Antarctic Research Expedition (JARE 53) members for their support to the field activity. The tide data were provided by N. Izumi and the microscopic analysis of water sample was carried out by H. Endo. T. Iwami helped us to identify the animals found in the subshelf cavity. Drilling equipment was constructed by the workshop of the Institute of Low Temperature Science, Hokkaido University. The quality of the paper was substantially improved by insightful comments from K. Christianson and an anonymous reviewer. Thanks are extended to S. Imura for his contribution to the project, to H. Blatter and R. Greve for their comments on the manuscript, and to P. Shearer for handling the paper as the Scientific Editor. This research was a scientific program of JARE 53 and partly funded by JSPS KAKENHI Grant Number 23651002 (2011–2013) and 23403006 (2011–2014).

Appendix A. Supplementary material

Supplementary data associated with this article can be found in the online version at http://dx.doi.org/10.1016/j.epsl.2014.05.001. These data include videos filmed in the subshelf water cavity and the Google map of the most important areas described in this article.

References

Alley, R.B., Anandakrishnan, A., Dupont, T.K., Parizek, B.R., Pollard, D., 2007. Effect of sedimentation on ice-sheet grounding-line stability. Science 315, 1838–1841. http://dx.doi.org/10.1126/science.1138396.

Anandakrishnan, A., Catania, G.A., Alley, R.B., Horgan, H.J., 2007. Discovery of till deposition at the grounding line of Whillans Ice Stream. Science 315, 1835–1838. http://dx.doi.org/10.1126/science.1138393.

Bindschadler, R., et al., 2011. Getting around Antarctica: new high-resolution mapping of the grounded and freely-floating boundaries of the Antarctic ice sheet created for the International Polar Year. Cryosphere 5, 569–588. http://dx.doi.org/10.5194/tc-5-569-2011.

Bogorodsky, V.V., Bentley, C.R., Gudmandsen, P.E., 1985. Radioglaciology. D. Riedel Publishing Company, Dordrecht.

Christianson, K., et al., 2013. Ice sheet grounding zone stabilization due to till compaction. Geophys. Res. Lett. 40, 5406–5411. http://dx.doi.org/10.1002/2013GL057447.

Dutrieux, P., et al., 2014. Strong sensitivity of Pine Island Ice-Shelf melting to climatic variability. Science 343, 174–178. http://dx.doi.org/10.1126/science.1244341.

Fricker, H.A., Padman, L., 2006. Ice shelf grounding zone structure from ICESat laser altimetry. Geophys. Res. Lett. 33, L15502. http://dx.doi.org/10.1029/2006GL026907.

Fricker, H.A., et al., 2011. Siple Coast subglacial aquatic environments: the Whillans Ice Stream subglacial access research drilling project. In: Siegert, M.J., Kennicutt, M.C. II, Bindschadler, R.A. (Eds.), Antarctic Subglacial Aquatic Environments. In: Geophys. Monogr., vol. 192. AGU, Washington, DC, pp. 199–219.

Fujino, K., Lewis, E.L., Perkin, R.G., 1974. The freezing point of seawater at pressures up to 100 bars. J. Geophys. Res. 79 (12), 1792–1797. http://dx.doi.org/10.1029/JC079i012p01792.

Fukuchi, M., Tanimura, A., Ohtsuka, H., Hoshiai, T., 1985. Marine biological data of BIOMASS programme at Syowa Station in the 1982 winter (JARE-23). Marine Biology 6, JARE Data Rep., vol. 98, pp. 1–113.

Fukuda, T., Sugiyama, S., Matoba, S., Shiraiwa, T., 2011. Glacier flow measurement and radio-echo sounding at Aurora Peak, Alaska in 2008. Ann. Glaciol. 52 (58), 138–142. http://dx.doi.org/10.3189/172756411797252130.

Fukuda, T., Sugiyama, S., Sawagaki, T., Nakamura, K., 2014. Recent variations in the terminus position, ice velocity and surface elevation of the Langhovde Glacier, East Antarctica. Antarct. Sci. 26, in press.

Gutt, J., et al., 2011. Biodiversity change after climate-induced ice-shelf collapse in the Antarctic. Deep-Sea Res., Part II 58, 74–83. http://dx.doi.org/10.1016/j.dsr2.2010.05.024.

Hattermann, T., Nost, O.A., Lilly, J.M., Smedsrud, L.H., 2012. Two years of oceanic observations below the Fimbul Ice Shelf, Antarctica. Geophys. Res. Lett. 39, L12605. http://dx.doi.org/10.1029/2012GL051012.

Held, C., Wägele, J.-W., 2005. Cryptic speciation in the giant Antarctic isopod *Glyptonotus antarcticus* (*Isopoda*: *Valvifera*: *Chaetiliidae*). Sci. Mar. 69 (Suppl. 2), 175–181.

Holland, P.R., 2008. A model of tidally dominated ocean processes near ice shelf grounding lines. J. Geophys. Res. 113, C11002. http://dx.doi.org/10.1029/2007JC004576.

Horgan, H.J., Christianson, K., Jacobel, R.W., Anandakrishnan, S., Alley, R.B., 2013a. Sediment deposition at the modern grounding zone of Whillans Ice Stream, West Antarctica. Geophys. Res. Lett. 40, 3934–3939. http://dx.doi.org/10.1002/grl.50712.

Horgan, H.J., et al., 2013b. Estuaries beneath ice sheets. Geology 41 (11), 1159–1162. http://dx.doi.org/10.1130/G34654.1.

Hubbard, B., Glasser, N., 2005. Field Techniques in Glaciology and Glacial Geomorphology. John Wiley & Sons Ltd, Chichester, UK.

Jacobs, S.S., Helmer, H.H., Doake, C.S.M., Jenkins, A., Frolich, R.M., 1992. Melting of ice shelves and the mass balance of Antarctica. J. Glaciol. 38 (130), 375–387.

Jacobs, S., Jenkins, A., Giulivi, C.F., Dutrieux, P., 2011. Stronger ocean circulation and increased melting under Pine Island Glacier ice shelf. Nat. Geosci. 4, 519–523. http://dx.doi.org/10.1038/ngeo1188.

Jamieson, S.S.R., Vieli, A., Livingstone, S.J., Cofaigh, C.Ó., Stokes, C., Hillenbrand, C.-D., Dowdeswell, J.A., 2012. Ice-stream stability on a reverse bed slope. Nat. Geosci. 5, 799–802. http://dx.doi.org/10.1038/ngeo1600.

Jenkins, A., 1991. A one-dimensional model of ice shelf-ocean interaction. J. Geophys. Res. 96 (C11), 20671–20677. http://dx.doi.org/10.1029/91JC01842.

Jenkins, A., Doake, C.S.M., 1991. Ice–ocean interaction on Ronne Ice Shelf, Antarctica. J. Geophys. Res. 96 (C1), 791–813. http://dx.doi.org/10.1029/90JC01952.

Jenkins, A., Corr, H.F.J., Nicholls, K.W., Steward, C.L., Doak, C.S.M., 2006. Interaction between ice and ocean observed with phase-sensitive radar near an Antarctic ice-shelf grounding line. J. Glaciol. 52 (178), 325–346. http://dx.doi.org/10.3189/172756506781828502.

Jezek, K.C., Clough, J.W., Bentley, C.R., Shabatie, S., 1978. Dielectric permittivity of glacier ice measured in situ by radar wide-angle reflection. J. Glaciol. 21 (85), 315–329.

Le Brocq, A.M., et al., 2013. Evidence from ice shelves for channelized meltwater flow beneath the Antarctic Ice Sheet. Nat. Geosci. 6, 945–948. http://dx.doi.org/10.1038/ngeo1977.

Lipps, J.H., Ronan Jr., T.E., Delaca, T.E., 1979. Life below the Ross Ice Shelf. Science 203, 447–449. http://dx.doi.org/10.1126/science.203.4379.447.

MacAyeal, D.R., 1984. Thermohaline circulation below the Ross Ice Shelf: a consequence of tidally induced vertical mixing and basal melting. J. Geophys. Res. 89 (C1), 597–606. http://dx.doi.org/10.1029/JC089iC01p00597.

Miles, B.W.J., Stokes, C.R., Vieli, A., Cox, N.J., 2013. Rapid, climate-driven changes in outlet glaciers on the Pacific coast of East Antarctica. Nature 500, 563–566. http://dx.doi.org/10.1038/nature12382.

Moriwaki, K., Yoshida, Y., 1990. Bathymetric Chart of Lützow–Holmbukta (Antarctica). Special Map Series of National Institute of Polar Research, vol. 4.

Nicholls, K.W., et al., 2006. Measurements beneath an Antarctic ice shelf using an autonomous underwater vehicle. Geophys. Res. Lett. 33, L08612. http://dx.doi.org/10.1029/2006GL025998.

Nicholls, K.W., Makinson, K., Venables, E.J., 2012. Ocean circulation beneath Larsen C Ice Shelf, Antarctica from in situ observations. Geophys. Res. Lett. 39, L19608. http://dx.doi.org/10.1029/2012GL053187.

Ohshima, K.I., Kawamura, T., 1994. Oceanographic data in Lützow–Holm Bay of Antarctic climate research programme from January 1991 to February 1992 (JARE-32). Oceanography 15, JARE Data Rep., vol. 198, pp. 1–35.

Ohshima, K.I., Takizawa, T., Ushio, S., Kawamura, T., 1996. Seasonal variations of the Antarctic coastal ocean in the vicinity of Lützow–Holm Bay. J. Geophys. Res. 101 (C9), 20617–20628. http://dx.doi.org/10.1029/96JC01752.

Padman, L., Fricker, H.A., Coleman, R., Howard, S., Erofeeva, L., 2002. A new tide model for the Antarctic ice shelves and seas. Ann. Glaciol. 34, 247–254.

Powell, R.D., Dawber, M., McInnes, N., 1996. Observations of the grounding-line area at a floating glacier terminus. Ann. Glaciol. 22, 217–223.

Pritchard, H.D., Ligtenberg, S.R.M., Fricker, H.A., Vaughan, D.G., van den Broeke, M.R., Padman, L., 2012. Antarctic ice-sheet loss driven by basal melting of ice shelves. Nature 484, 502–505. http://dx.doi.org/10.1038/nature10968.

Riddle, M.J., Craven, M., Goldsworthy, P.M., Carsey, F., 2007. A diverse benthic assemblage 100 km from open water under the Amery Ice Shelf, Antarctica. Paleoceanography 22, PA1204. http://dx.doi.org/10.1029/2006PA001327.

Rignot, R., Jacobs, S.S., 2002. Rapid bottom melting widespread near Antarctic ice sheet grounding lines. Science 296, 2020–2023. http://dx.doi.org/10.1126/science.1070942.

Rignot, E., Mouginot, J., Scheuchl, B., 2011. Antarctic grounding line mapping from differential satellite radar interferometry. Geophys. Res. Lett. 38, L10504. http://dx.doi.org/10.1029/2011GL047109.

Rignot, E., Jacobs, S., Mouginot, J., Scheuchl, B., 2013. Ice-shelf melting around Antarctica. Science 341, 266–270. http://dx.doi.org/10.1126/science.1235798.

Schoof, C., 2007. Ice sheet grounding line dynamics: steady states, stability, and hysteresis. J. Geophys. Res. 112 (B9), F03S28. http://dx.doi.org/10.1029/2006JF000664.

Smith, A.M., 1991. The use of tiltmeters to study the dynamics of Antarctic ice-shelf grounding lines. J. Glaciol. 37 (125), 51–58.

Stephenson, S.N., 1984. Glacier flexure and the position of grounding lines: measurements by tiltmeter on Rutford ice stream, Antarctica. Ann. Glaciol. 5, 165–169.

Stearns, L.A., Smith, B.E., Hamilton, G.S., 2008. Increased flow speed on a large East Antarctic outlet glacier caused by subglacial floods. Nat. Geosci. 1, 827–831. http://dx.doi.org/10.1038/ngeo356.

Sugiyama, S., Skvarca, P., Naito, N., Tone, K., Enomoto, H., Shinbori, K., Marinsek, S., Aniya, M., 2010a. Hot-water drilling at Glaciar Perito Moreno, Southern Patagonia Icefield. Bull. Glaciol. Res. 29, 27–32.

Sugiyama, S., Bauder, A., Riesen, P., Funk, M., 2010b. Surface ice motion deviating toward the margins during speed-up events at Gornergletscher, Switzerland. J. Geophys. Res. 115, F03010. http://dx.doi.org/10.1029/2009JF001509.

Sugiyama, S., Skvarca, P., Naito, N., Enomoto, H., Tsutaki, S., Tone, K., Marinsek, S., Aniya, M., 2011. Ice speed of a calving glacier modulated by small fluctuations in basal water pressure. Nat. Geosci. 4, 597–600. http://dx.doi.org/10.1038/ngeo1218.

Thoma, M., Jenkins, A., Holland, D., Jacobs, S., 2008. Modelling Circumpolar Deep Water intrusions on the Amundsen Sea continental shelf, Antarctica. Geophys. Res. Lett. 35, L18602. http://dx.doi.org/10.1029/2008GL034939.

Tsutaki, S., Sugiyama, S., Nishimura, D., Funk, M., 2013. Acceleration and flotation of a glacier terminus during a proglacial lake formation in Rhonegletscher, Switzerland. J. Glaciol. 59 (215), 559–570. http://dx.doi.org/10.3189/2013JoG12J107.

Ushio, S., Takizawa, T., 1993. Oceanographic data in Lützow–Holm Bay of Antarctic climate research programme from March 1990 to January 1991 (JARE-31). Oceanography 13, JARE Data Rep., vol. 184, pp. 1–34.

Weertman, J., 1974. Stability of the junction of an ice sheet and an ice shelf. J. Glaciol. 13 (67), 3–11.

Whitworth, T., Orsi, A.H., Kim, S.J., Nowlin, W.D., Locarnini, R.A., 1998. Water masses and mixing near the Antarctic slope front. In: Jacobs, S.S., Weiss, R.F. (Eds.), Ocean, Ice, and Atmosphere: Interactions at the Antarctic Continental Margin. In: Antarct. Res. Ser., vol. 75. AGU, Washington, DC, pp. 1–27.